

Particle dynamics in the rising plume at Piccard Hydrothermal Field, Mid-Cayman Rise

M. L. Estapa^{1*}, J. A. Breier^{1**}, C. R. German¹

¹ Woods Hole Oceanographic Institution, Woods Hole, MA

* *Present address:* Department of Geosciences, Skidmore College, Saratoga Springs, NY

** *Present address:* School of Multidisciplinary Studies, University of Texas Rio Grande Valley,
Brownsville, TX

Corresponding author: M. L. Estapa, Department of Geosciences, Skidmore College, 815 N.

Broadway, Saratoga Springs, NY, 12866, USA, mestapa@skidmore.edu

This article has been accepted for publication and undergone full peer review but has not been through the copyediting, typesetting, pagination and proofreading process which may lead to differences between this version and the Version of Record. Please cite this article as doi: 10.1002/2015GC005831

© 2015 American Geophysical Union

Received: Apr 01, 2015; Revised: Jun 30, 2015; Accepted: Jul 01, 2015

Particle dynamics in the rising plume at Piccard Hydrothermal Field, Mid-Cayman Rise

M. L. Estapa^{1*}, J. A. Breier¹, C. R. German¹

¹ Woods Hole Oceanographic Institution, Woods Hole, MA

* *Present address:* Department of Geosciences, Skidmore College, Saratoga Springs, NY

Corresponding author: M. L. Estapa, Department of Geosciences, Skidmore College, 815 N. Broadway, Saratoga Springs, NY, 12866, USA, mestapa@skidmore.edu

Highlights:

- Particles less than 30 μm dominated the rising Beebe plume
- Plume particle size and composition varied strongly over narrow depth layers
- Particle properties can be measured by optical proxy in hydrothermal plumes

Abstract: Processes active in rising hydrothermal plumes, such as precipitation, particle aggregation, and biological growth, affect particle size distributions and can exert important influences on the biogeochemical impact of submarine venting of iron to the oceans and their sediments. However, observations of particle size distribution within these systems, to date, are both limited and conflicting. In a novel buoyant hydrothermal plume study at the recently discovered high-temperature (398°C) Piccard Hydrothermal Field, Mid-Cayman Rise, we report optical measurements of particle size distributions (PSDs). We describe the plume PSD in terms of a simple, power-law model commonly used in studies of upper- and coastal ocean particle dynamics. Observed PSD slopes, derived from spectral beam attenuation and laser diffraction measurements, are among the highest found to date anywhere in the ocean and ranged from 2.9 to 8.5. Beam attenuation at 650 nm ranged from near zero to a rarely-observed maximum of 192 m⁻¹ at 3.5 m above the vent. We did not find large (>100 μm) particles that would settle rapidly to the sediments. Instead, beam attenuation was well-correlated to total iron, suggesting the first-order importance of particle dilution, rather than precipitation or dissolution, in the rising plume at Piccard. Our observations at Piccard caution against the assumption of rapid deposition of hydrothermal, particulate metal fluxes, and illustrate the need for more particle size and composition measurements across a broader range of sites, globally.

Keywords: Hydrothermal particulate iron fluxes, particle size distribution, particle inherent optical properties, *in situ* optical sensors, Mid-Cayman Rise, Piccard Hydrothermal Field

1. Introduction

The flux of hydrothermal iron to the ocean is comparable to the riverine Fe flux [Elderfield and Schultz, 1996]. However, the biogeochemical fates of hydrothermal metals in the water column depend on competing rates of particle formation, dissolution, and deposition [German & Seyfried, 2014]. A growing number of studies show the ubiquitous presence of hydrothermal, dissolved iron in the deep ocean [Klunder et al., 2011, 2012; Wu et al. 2011; Nishioka et al., 2013; Saito et al., 2013; Conway et al, 2014; Fitzsimmons et al., 2014a; Sedwick et al., 2014; Hatta et al., 2015]. This hydrothermal iron may be maintained in the water column as nano-particulates, or through organic complexation [Bennett et al., 2008; Sander and Koschinsky, 2011; Yücel et al., 2012; Hawkes et al., 2013; Gartman et al., 2014]. A significant fraction of small (micron or submicron) iron-containing particles may escape near-vent sedimentation, eventually contributing to the hydrothermally-sourced, dissolved pool. For instance, hydrothermal iron oxide particles have been detected in the water column far from vents [Baker et al., 1985; Ohnemus and Lam, 2015; Fitzsimmons et al., 2014b]. Near-vent measurements have indicated the presence of significant fractions of particles with diameters less than 2 μm [Walker and Baker 1988] and pyrite nanoparticles [Yücel et al., 2012; Gartman et al. 2014] whose oxidative dissolution rates are slow enough [Feely et al., 1987; Gartman and Luther, 2014] to suggest long term (months to years) persistence in the water column. These particles, with diameters less than order 2 μm , have Stokes' settling velocities less than 1 m d^{-1} and could potentially contribute to pelagic ocean biogeochemical cycling. They also exert control on distributions of phosphorus and chalcophile elements early in the rising plume [Sands et al., 2012]. At some sites, rising hydrothermal plumes also carry very large particles, 100 μm and larger [Feely et al. 1987; 1990]. Such large particles would be unlikely to travel more than a few

kilometers before deposition in the sediments and/or re-entrainment into buoyant hydrothermal plumes [Feely et al., 1987; German & Sparks, 1993].

Clearly, the mass distribution of hydrothermal metal fluxes among particles of different sizes has important implications for the biogeochemical fate of those metals in the ocean. Dissolved and small iron-containing particles that are not lost quickly to sedimentation have greater opportunities for organic stabilization [Bennett et al., 2008; Toner et al. 2009; Breier et al. 2012] and persistence in the deep ocean. However, particle size distribution measurements in the rising hydrothermal plume are rare and challenging to make. Feely et al. [1987, 1990] used optical and scanning electron microscopy to characterize Juan de Fuca ridge plume particles, and reported the size ranges (order 0.1 – 100 μm) and maximum diameters (usually order 100 μm). They modeled particle transport distances for the upper end of their observed diameter ranges (order 10-100 μm). However, they did not report the numerical or equivalent volume size distributions of their samples [Feely et al., 1990] which limits our ability to assess the importance of particles larger than 100 μm to overall elemental fluxes from the vent. Walker and Baker [1988] used a Coulter counter to measure plume particle size distributions in the Juan de Fuca ridge neutrally-buoyant plume. Their method had an upper particle diameter cutoff of 10 μm , but their reported size distributions, if extrapolated to larger size classes, would be consistent with most particle mass being present at micron or submicron sizes. This inferred distribution argues against the sedimentation of large particles controlling the fate of particulate metals injected by vents in the deep ocean [Feely et al., 1990]. At the East Pacific Rise, Breier et al. [2012] also observed particles ranging in size from less than 0.02 to greater than 10 μm using scanning transmission X-ray microscopy of neutrally-buoyant plume particles filtered *in situ*. The limited number of

observations using different methodologies complicates efforts to understand the ultimate fate of particulate, hydrothermal metals in the ocean.

Particle size and composition are likely to evolve quickly, on timescales of seconds to minutes and spatial scales of centimeters to meters [Breier et al., 2012]. All of the particle size measurements discussed above were limited by observational methods requiring discrete sampling and labor-intensive analyses. However, simple, commercially-available, optical sensors have been broadly used in hydrothermal plumes for several decades to provide continuous, *in situ*, qualitative and quantitative measures of particle concentration [e.g., Baker et al., 2001]. More complex sensors are also used in a variety of surface ocean settings where they also provide proxy information about particle size and composition [Boss et al, 2015]. Here, we briefly discuss and apply two optical proxies for particle size which were developed in the upper ocean but whose utility has not yet, to our knowledge, been demonstrated in hydrothermal plumes. They are 1) the spectral slope of beam attenuation [Kitchen et al., 1982; Voss, 1992; Boss et al., 2001a,b]; and 2) near-forward angle laser diffraction [Agrawal and Pottsmith, 2000; Agrawal et al., 2008]. We also investigate the applicability of optical property ratios, specifically the sidescattering to beam attenuation ratio, as qualitative proxies for particle size and composition. The theoretical frameworks and surface ocean applications of these methods are well-described in the literature, so here we give only brief summaries. We then present new optical observations from the Piccard Hydrothermal Field, Mid-Cayman Rise, a high-temperature site that lies nearly 5,000 m deep [German et al., 2010] and offer suggestions for future use of these optical proxies in other hydrothermal plume studies.

2. Particle size distribution models and optical proxies for particle size

2.1. Particle size distribution models

In typical oceanic waters, the particle size distribution (PSD) has often been approximated using a power-law function (or Junge size distribution),

$$N(D) = N(D_o)(D/D_o)^{-\xi} \quad (\text{Eq. 1})$$

where $N(D)$ is the number concentration of particles of diameter D , D_o is a reference diameter, and ξ the PSD slope [Junge 1969; Sheldon et al. 1972]. In much of the ocean's interior, particulate volume is distributed approximately equally among logarithmically-spaced size classes, equivalent to a number size distribution with $\xi = 4$ (and volume size distribution with $\xi = 3$) in the power-law model [Sheldon et al., 1972]. In hydrothermal vent plumes, the power-law model has also been applied [Walker and Baker 1988], although few measurements of the PSD exist for this type of environment. McCave [1984] suggested that the “flat”, power-law volume-size distribution reflects a steady-state equilibrium between particle aggregation and disaggregation processes. Departures from the power-law size distribution would thus be observed closer to particle source regions [McCave 1984]. Controls on aggregation and disaggregation include particle concentration, collision efficiency, and collision frequency [McCave 1984; Jackson and Burd 1998]. Brownian motion, turbulent shear, and differential sedimentation all affect collision frequency, with the variable importance of these processes for different particle sizes also leading to departures from a power-law PSD [McCave 1984]. Uniquely in the ocean, high-temperature vent plumes feature rapid formation of very small mineral particles (crystal unit cells have sizes of tens of nanometers) due to precipitation in vent

fluids. Buoyant plumes also feature strong turbulent diffusivities and lateral gradients in turbulent shear [Jiang and Breier 2014]. Both of these factors could lead to extreme values of ξ or departures from the power-law PSD model.

2.2. Beam attenuation spectral slope

The spectral slope of beam attenuation, γ , describes the wavelength-dependence of the spectral, particulate beam attenuation coefficient $c_p(\lambda)$, which in the upper ocean is well-approximated by a power-law function [Boss et al., 2001a]. Boss et al. [2001a; b] have described in detail the theoretical relationship between γ and ξ , its derivation, and applicability as a proxy in various oceanic particle populations. *In situ* measurements of γ are routinely made with commercially-available, reflecting-tube, spectral beam attenuation meters [Zaneveld et al., 1994] and inverted to obtain ξ [Boss et al., 2001a; b]. Departures from the theoretical relationship between γ and ξ are possible in populations of particles that absorb light strongly. These departures are strongest when ξ values are large (i.e. there are many small particles) and when the real part of the particles' refractive index (n) is low, which is not the case for mineral particles in hydrothermal plumes. Boss et al. [2001a] found that for particles with $n = 1.2$, inverted ξ values were only minimally affected for $\xi < 4.5$.

2.3. Laser diffraction at near-forward angles

As particles increase in size, they scatter light through increasingly near-forward angles, and this dependence on size is relatively insensitive to particle composition [Agrawal and Pottsmith 2000]. Laser-diffraction instruments such as the commercially-available Laser In-Situ Scattering and Transmissometry (LISST) meter (Sequoia Scientific; Agrawal and Pottsmith, 2000) use

these properties to provide *in situ* particle-size distribution information over particle diameters ranging from order 1 to 100 microns. The measured angular scattering signal is inverted based on modeled, theoretical scattering by spheres [Agrawal and Pottsmith, 2000] or using an empirical scattering matrix derived from measurements of irregularly-shaped coastal and riverine sediments [Agrawal et al. 2008].

2.4. Optical property ratios

Light attenuation and scattering by marine particles vary, to first order, with particle concentration. Ratios of two optical properties provide second-order information about the composition and size of particles. By definition, beam attenuation includes light scattering integrated over all angles. In practice, however, transmissometers have finite detector acceptance angles, so measured c_p excludes some light scattered in extreme, near-forward directions [Boss et al., 2009]. In contrast, backscattering and sidescattering sensors collect only a portion of the light scattered through larger angles. While scattering by particles large relative to the wavelength of visible light (i.e., order 10 to 100 μm) enhances scattering through near-forward angles as discussed above, small particles (i.e., order 0.1 – 10 μm) have enhanced scattering through angles greater than 90° [Stramski and Kiefer, 1991; Stramski et al., 2001]. Higher-refractive index particles (mineral rather than organic) also have higher relative backscattering [Twardowski et al., 2001; Loisel et al., 2007; Neukermans et al., 2012]. Therefore, ratios of two optical properties with different scattering responses (e.g., backscattering to beam attenuation) provide information on particle size and composition [Sullivan et al., 2005; Loisel et al., 2007; Cetinic et al. 2012; Neukermans et al., 2012].

To our knowledge, optical property ratios have not previously been used, rigorously, as size or compositional proxies in deep-sea hydrothermal plumes. Baker et al. [2001] published a set of mass concentration-normalized backscattering measurements from Axial Volcano, where they attributed higher-than-expected, mass-normalized backscattering in some samples to particle shape effects. This is consistent with rapid evolution of particle size and composition under kinetic control in the rising plume [Breier et al., 2014]. The backscattering sensor utilized by Baker et al. [2001] (LBSS, WETLabs) has been supplanted in many recent plume studies by the LSS turbidity sensor (Seapoint), which measures sidescattering over a broader angular range but still should, in theory, be more sensitive than beam attenuation to small, inorganic particles. Hence, we investigate here the applicability of the sidescattering/ c_p ratio within the rising hydrothermal plume as a potentially useful, qualitative particle size and composition proxy.

3. Methods

3.1 Study site and deployment design

The measurements presented here were all collected directly above the Beebe Vents mound which hosts a cluster of five active black-smoker chimneys. This site is located at 18.5467° N 81.7184° W, 4960m water depth, within the larger Piccard Hydrothermal Field on the ultra-slow spreading Mid Cayman Rise [Kinsey & German, 2013]. Our observations were collected from two separate platforms during cruise FK008 of the *R/V Falkor* in June 2013 [German, 2014]. A Seabird 9/11+ CTD-rosette was used to make *in situ* measurements of beam attenuation (WETLabs C-Star transmissometer, 25 cm pathlength, 650 nm) and side-scattering (Seapoint LSS, 880 nm) above and within the rising plume down to about 50 m above bottom. The CTD-

rosette was also used to collect complementary bottle samples during the upcast only, for additional optical analyses aboard ship (described below). The data reported here come from both the upcast and downcast, which were separated in time by a few minutes, but (as is typical) intersected the plume spatially in different locations due to horizontal motion of the rosette relative to the plume. The *HROV Nereus* [Bowen et al., 2008] and SUPR sampling system [Breier et al., 2009; Breier et al., 2014] were used 0-50 m above the mouth of Beebe Vent #4 to collect bottle samples, which were also returned to the ship for optical and whole-water (unfiltered) iron measurements (described below).

3.2 Instrumentation and calibration

The C-Star and LSS sensors were mounted near the bottom of the rosette frame at the same vertical position and were cleaned with pure water (MilliQ Direct8) and lint-free tissue prior to each cast. The C-Star was mounted horizontally in an open-path configuration. Both sensors' air calibrations remained stable throughout the cruise. In addition to the C-Star and LSS sensors carried aboard the CTD, a multispectral beam attenuation meter (ac9, WETLabs) and laser-diffraction particle size meter (LISST-100X Type C, Sequoia Scientific) were used aboard the ship to analyze discrete samples. The measurements were made on the ship because the instruments lacked adequate pressure casings for in situ use. Both sensors are also commercially available in deep-rated housings. The LISST measured particle sizes in 32 log-spaced size bins ranging from 2.5 – 500 μm , across an optical pathlength of 5 cm, at a wavelength of 650 nm. It was equipped with a ~140 mL flow-through sample chamber used for sample analysis and for periodic, pure-water “zscat” readings. The ac9 had an optical pathlength of 25 cm and nominal wavelengths of 412, 440, 480, 510, 532, 555, 650, 676, and 715 nm. The ac9 normally is used to

measure both absorption and beam attenuation, but the absorption light source failed early in the cruise, so we report only spectral beam attenuation here. Additionally, due to instrument scheduling constraints, the ac9 was only used with CTD bottle samples collected during the first leg of our field expedition. It should also be noted, however, that the ac9's 25 cm pathlength would likely have been too long for use with the high-turbidity, near-vent *Nereus*-SUPR bottle samples that were collected from close above the vents during the second leg of our research cruise. Pure-water offsets for the ac9 were recorded throughout the cruise and sample attenuation was corrected for the temperature-dependence of pure-water absorption [Sullivan et al., 2006]. Deep-water offsets (~3,000 m, well above the ~4100 m deep non-buoyant plume; German et al., 2010) were subtracted from both the C-Star and ac9 readings to intercalibrate the two sensors.

3.3 Optical sample collection and analysis

Discrete samples were collected from Niskin (CTD) and SUPR (*Nereus*) bottles directly into gas-tight, 140 mL syringes equipped with 3-way valves in order to protect them from oxidation. After equilibrating at room temperature, samples were introduced into the ac9 and LISST directly from the syringes through 1/8" ID Tygon tubing. Samples for ac9 analysis were collected in pairs, with one of each pair additionally passed through a 0.2 μm syringe filter (Millipore, Sterivex-GP, polyethersulfone) during introduction to the instrument in order to obtain matrix-matched, particle-free attenuation spectra. Near-vent samples for LISST analysis occasionally were so turbid as to require dilution (done in the syringes using <0.2 μm sample filtrate) to achieve target transmissions between 0.3 and 0.9. Particulate beam attenuation at 650 nm ($c_p(650)$) from the LISST was corrected as necessary for these dilutions. Both ac9 and

LISST data were collected for 1-2 minutes per sample, the LISST without averaging.

Multispectral beam attenuation data were median-filtered to remove rare spikes and averaged over the 1-2 minute recording period. Uncertainty was computed as the difference between the 85th and 15th percentiles of the timeseries. The particulate beam attenuation spectrum ($c_p(\lambda)$) was calculated as the difference between the median unfiltered and filtered spectra for each sample. Raw LISST data were inverted using Sequoia Scientific's randomly-shaped particle matrix [Agrawal et al. 2008] to obtain the volume size distribution. This was converted to a number size distribution (NSD) by dividing by the equivalent spherical volume per particle and by the size bin width. The median NSD was computed from the timeseries and the uncertainty computed as the difference between the 85th and 15th percentiles. Size bins where the median was less than twice the uncertainty were flagged and removed from particle size distribution analysis. This was common for particle sizes greater than about 30 microns, indicating that those larger particles were too rare in the 140 mL samples for reliable detection. The smallest size bin was also discarded to avoid aliasing from particles outside the instrument's detection range.

3.4 Whole-water iron sample collection and analysis

Whole water (unfiltered) sample aliquots (500 mL) from the SUPR bottles were acidified to a pH of 1.7 with concentrated nitric acid and stored for 6 months at room temperature prior to analysis. The resulting *total dissolvable* iron (TDFe) concentrations in these whole water sample aliquots were measured by the ferrozine spectrophotometric method on a Hach DR 3800 spectrophotometer [Stookey et al., 1970].

3.5 Particle size proxy computations

The γ parameter was determined from $c_p(\lambda)$ spectra using a non-linear, least-squares minimization (MATLAB function “fminsearch”). A Monte Carlo approach was used to propagate $c_p(\lambda)$ uncertainty into the derived γ estimates. Values of ξ were computed from γ following Boss et al. [2001a]. A fitting approach similar to that used for γ was used to determine ξ from the LISST number size distributions. In some samples, the median particle number concentration was smaller than the uncertainty in nearly all size bins, prohibiting estimation of ξ .

The LSS side-scattering sensor on the CTD did not have a defined measurement angle, but collected sidescattered light at angles between 15-150°, with peak response at 90° [LSS Datasheet, Seapoint, Inc.]. As only one sensor was in use during this project, we did not perform a calibration against reference particles such as polystyrene beads or a formazine suspension (which would be required to report nephelometric turbidity units and to compensate for small sensor-to-sensor differences; Baker et al., 2001). Instead, we linearly transformed the raw LSS signal voltage to scale with the calibrated values of $c_p(650)$ from the C-Star. We computed the scaling parameters by regressing the raw LSS signal against depth-aligned $c_p(650)$, using all data below 1000 m. We then computed the ratio of the scaled LSS voltage to $c_p(650)$, and propagated the instrument resolution uncertainty into the ratio.

4. Results

4.1 Beam attenuation magnitude

Beam attenuation in the *rising* plume above the Beebe Vents mound decreased by 3 orders of magnitude from 0.5 - 250 m above the vent (Fig. 1a; note that all data presented here are situated

well below the depth of the non-buoyant dispersing plume at *Piccard* which lies at $\sim 4,100$ m depth, more than 800m above the vent-source at the seabed [German et al., 2010]]. The *in situ* C-Star and corresponding discrete, $c_p(650)$ measurements agreed within instrumental uncertainty, both within the rising plume (Fig. 1a) and above its influence (not shown). Downcast $c_p(650)$ and LSS voltage values were approximately a factor of 5 smaller than on the upcast. Downcast temperatures (not shown) were also closer to background values than on the upcast, suggesting that the upcast passed closer to the axis of the buoyant plume rising above the Beebe Vents mound. Spectral attenuation by $0.2 \mu\text{m}$ -filtered CTD samples was always small compared to attenuation in unfiltered samples. CTD samples, all of which were collected from higher in the rising plume, produced insufficient signal in the 5 cm-pathlength LISST to warrant further analysis. The *Nereus* dive during which LISST samples were collected occurred 19 days after the corresponding CTD cast, so measurements were not continuous, but the order of magnitude of $c_p(650)$ remained the same in the overlapping 4875-4920 m depth range for the two deployments (Fig. 1a). Samples collected 0.5 – 30 m above the vent had $c_p(650)$ ranging through two orders of magnitude (Fig. 1a), with a maximum value of 192 m^{-1} after correction for dilution. This maximum, 3.5 m above the vent, exceeded observations immediately above the mouth of the vent (+0.5 m, 65 m^{-1}).

4.2 Particle size and composition proxies

Particulate beam attenuation spectra from CTD samples were well-described by the power-law model (Eq. 1), and their ξ values varied from 3.9 to 4.6 (open circles, Fig.1b). The samples with the flattest particle size distribution (PSD) slopes (smallest ξ) also had the lowest $c_p(\lambda)$ magnitudes (Fig. 1a, b) and exhibited a poorer fit to the power-law model at wavelengths above

650 nm (data not shown]. Computed ξ values did not strongly depend on inclusion or exclusion of these red wavelengths from the least-squares minimization. In these CTD samples, ξ generally increased slowly with increasing depth within the buoyant plume, albeit with a local excursion to a lower value at 4855 m (Fig. 1b). Boss et al. [2001a] found that for light-absorbing particles with refractive indices (n) of 1.2, the γ -inversion model overestimated ξ by approximately 0.1 for $\xi = 4.6$. While we do not know the refractive index of particles in the Beebe plume, if they are minerals originating in precipitating vent fluids it is likely they have n of 1.2, or even higher.

The *in situ* ratio of scaled LSS output to $c_p(650)$ ($LSS:c_p$) exhibited strong variability over narrow depth layers, approximately 10 m thick, throughout the lower segment of the rising plume that was sampled via CTD (Figure 1c). These narrow layers were more prevalent on the downcast than on the upcast. The local depth-minimum in ξ , derived independently from bottle sample measurements at 4855m, coincided with a minimum in upcast $LSS:c_p$ at that depth, but not all minima in the $LSS:c_p$ profiles coincided with minima in ξ (Fig. 1b, c).

LISST particle size spectra were obtained from a suite of *Nereus*-SUPR bottle samples collected within approximately 50 m of the vent mouth (Fig. 2). Values of ξ were computed for the subset of samples (0.5 – 3.5 and 36.5 m above the vent) that had well-resolved particle number concentrations within the LISST's 2.5 to 500 μm size range. Particle counts in size bins larger than 30 μm were only rarely larger than zero. The particle number size distributions were well-approximated by the power-law model (Eq. 1) in the 5-30 μm range (Fig. 2), but departed from it below diameters of 5 μm (Fig. 2). Values of ξ fit from 5-30 μm ranged from 3.7-8.5, with the steepest PSD slopes observed 1.5-3.5 m above the vent and coinciding with maximum values of

$c_p(650)$ and TDFe (Fig. 3a,c). The median particle size ranged between 3.7 – 5.9 μm in the range 0.5 – 3.5 m above the vent, and increased to 13.4 μm at 36.5 m above the vent (Figure 3b).

4.3 Whole-water iron concentration

The below-plume, background, TDFe concentration was 1.58 nmol-Fe kg^{-1} . Within the plume, the TDFe concentration ranged from a maximum of 673 nmol-Fe kg^{-1} at 2.5 m above the vent (Fig. 3b), to a minimum of 0.66 nmol-Fe kg^{-1} at a distance of 49.5 m above the vent. Total dissolvable iron showed an approximately linear relationship with $c_p(650)$ ($R^2 = 0.96$, $n = 14$; Fig. 4a). At TDFe concentrations below 10 nmol-Fe kg^{-1} , however, the slope of this relationship steepened by over a factor of two ($R^2 = 0.998$ $n = 6$; Fig. 4b). Samples at 47-50 m above the vent departed from this trend.

5. Discussion

5.1 Interpretation of size proxies in context of plume dynamics and chemical fluxes

Inputs from immediately adjacent vent orifices with different heights likely caused the high and variable values of TDFe and $c_p(650)$ observed in SUPR bottle samples collected through the first 3.5 m of the plume rising above Beebe Vent #4 (Fig. 3b). The maximum TDFe value observed at 2.5 m was approximately equivalent to a 1:10 dilution of the Beebe Vents' fluid endmember (6.5-6.7 mmol-Fe kg^{-1} ; McDermott 2015). Above 3.5 m, visual evidence suggested that the plumes from all five high-temperature Beebe Vents had become well-mixed. Through the first 72.5m of the rising plume, TDFe and $c_p(650)$ were well-correlated in most samples (Fig. 4a), suggesting little repartitioning of iron (i.e., through precipitation and dissolution) between populations of particles large enough to scatter light (i.e., with diameters of the same order of

magnitude as the wavelength of light) and populations of particles, colloids, or truly dissolved phases too small to efficiently scatter light. Factors such as particle size may have contributed to second-order variability in the iron-normalized beam attenuation. For instance, relative to samples at 1.5-3.5 m, the 0.5 m sample contained larger particles (Fig. 3a,b) which could explain the slightly lower value of $c_p(650)$ relative to iron at 0.5 m (Fig. 4a; smaller particles more efficiently attenuate light; Stramski and Kiefer, 1991). Similarly, the doubling of the $c_p(650)$ vs. TDFe slope in most samples at greater plume heights (Fig. 4b) could be due to increased particle size, although only one PSD slope (ξ) measurement is available in that range (orange triangle, Fig. 3c). Finally, variability in the $c_p(650)$ vs. TDFe slope might reflect changes in the degree to which particulates absorb light as mineralogical composition evolves from sulfides to oxide phases, along oxidative and temperature gradients in the rising plume [Breier et al., 2012].

While we could not collect *in situ* light absorption data, laboratory ac-9 measurements of powdered mineral standards suspended in water (Fig. 5) showed clear differences in albedo (the fraction of beam attenuation due to scattering, rather than absorption of light) between iron sulfides and iron oxides.

Within the young rising plume, particle size distributions departed most strongly from the power-law model at particle diameters smaller than 5 μm (Fig. 2). The departure from a power law size spectrum suggests a disequilibrium among processes governing particle formation, dissolution, and aggregation, which would be less likely to produce a smooth particle size distribution [McCave, 1984]. One clear source of newly-formed particles is precipitation from vent fluids. We also observed that the smallest particles contributed more to the total particle volume in

samples collected between 1.5 – 3.5 m above the vent than they did either above or just below this layer (Fig. 4). This appears to be the zone of most rapid particle precipitation.

The normalized $LSS:c_p$ ratio qualitatively indicates relative particle size and refractive index.

Smaller, inorganic particles should have larger $LSS:c_p$ ratios, while larger, organic-rich particles should have smaller $LSS:c_p$ ratios. The coincidence of the minimum in the upcast $LSS:c_p$ ratio

with the minimum in ξ (Fig. 1, downcast 4,855) suggests the presence of larger particles, but could also be due to higher organic content associated with biological activity in the plume

[Bennett et al. 2011; Dick et al., 2013]. Observed $LSS:c_p$ maxima (Fig. 1c, downcast at 4740, 4760, 4775 and 4870 m; upcast at 4845m) suggest passage of the CTD through small eddies of

small, inorganic particles, each generally situated immediately adjacent to or between volumes with larger, possibly more organic-rich particles. The low-iron, high- $c_p(650)$ anomaly observed

49.5 m above the vent in the ROV bottle samples (Fig. 4b) could similarly reflect a small eddy of

particles of a different composition. Physical entrainment from multiple sources into the rising plume [Jiang and Breier, 2014] could drive these observations, whose optical-chemical property

ratios may reflect particles from a different chimney, reentrainment of more aged particles

[German and Sparks 1993] or microbially-enriched fluids emanating as diffuse flow from across the host Beebe Vents mound.

5.2 Sampling considerations

5.2.1 Schlieren effects

Specific considerations for *in situ* use of open-volume optical proxies near rising hydrothermal plumes include contamination of the signal by scattering of light through sharp refractive-index

gradients (the “schlieren effect”, visually recognizable as the “shimmer” seen close to the seafloor in and around sites of hot fluid discharge). This manifests as sharply increased beam attenuation or enhanced angular scattering in the near-forward direction ($< 1\text{-}2^\circ$) [Mikkelsen et al., 2008]. To check the possibility of such artifacts in our *in situ* observations, we empirically estimated the seawater refractive index gradient from temperature, salinity, and pressure [McNeil, 1977] and used Snell’s Law to compute maximal scattering angles and Fresnel reflectances along the gradient. Computed scattering angles were always smaller than 1.5° (the acceptance angle of the C-Star transmissometer) and reflectances less than 2.5×10^{-4} (equivalent to the instrument detection limit of 0.001 m^{-1}). Immediately above the vent orifice, however, this would not have been the case, accentuating the need for careful deployment design when preparing for any future *in situ* optical measurements.

5.2.2 CTD wake effects

Briggs et al. [2011] found differences between particle optical properties on CTD down- and upcasts in the upper ocean, consistent with disruption of fragile aggregates in the “wake” of the rosette (where optical sensors, as in this study, were mounted near the bottom of the frame). We observed upcast-downcast differences in LSS: c_p that we have attributed, primarily, to lateral movement of the CTD relative to the rising, turbulent hydrothermal plume, but may have also included rosette-wake effects.

5.2.3 Particle size distribution changes between collection and analysis

The unavoidable delay and exposure to background seawater temperatures ($\sim 3.9^\circ\text{C}$) between collection and shipboard analysis of discrete samples has always carried the potential to alter

hydrothermal particle properties. Here, we are encouraged that $c_p(650)$ values appeared unchanged between those measured during the CTD upcast in real time, *in situ* and those subsequently obtained shipboard, from discrete CTD-rosette samples (also collected during the upcast; Fig. 1a). We also took precautions against oxidative changes in our freshly-formed, buoyant plume samples by protecting them from air exposure during the time between sampling and shipboard measurements. Tube and syringe orifices were large enough to allow passage of particles up to 2 mm in diameter, although larger aggregates could have been disrupted. Future validation of particle size and composition proxies in recovered samples will require *in situ* measurements.

5.3 Comparison to literature observations

The $c_p(650)$ values measured in the first 10 m above the vent are, to our knowledge, among the highest ever recorded in the ocean and are consistent with the high sulfur and iron fluxes at this site [McDermott, 2015]. Values of ξ were also among the steepest observed in the marine environment, and consistent with those of Walker and Baker [1988] who observed $\xi = 7.5$ for particle diameters less than 1 μm , but with lower ξ at larger sizes, in Juan de Fuca ridge neutrally-buoyant plume particles. Our laser-diffraction observations in the rising plume above Beebe Vent #4 show a similar dominance of small particles, with high ξ values over a broad size range (microns to tens of microns), and low relative abundances of particles larger than order 10 μm . These observations suggest that at both of these sites, particulate mass fluxes in the young, rising plume may be dominated by slowly-settling particles.

The total, dissolvable iron and beam attenuation measurements in the Beebe Vent #4 rising plume imply that much of the light-scattering, iron-containing material is retained in the young, rising plume rather than lost to settling or dissolution. However, beam attenuation is most sensitive to primary particles with diameters of order 1-10 μm . Our LISST measurements from samples collected in the first few meters above the vent are consistent with most of the particles falling into size classes smaller than 10 μm (Fig. 4b). Even if these particles were solid (rather than aggregates with significant fluid volume) and made of pyrite (density 5.0 g cm^{-3}), their Stokes settling velocities would be less than approximately 1 m h^{-1} . In samples closest to the mouth of the vent, we did not observe any evidence for large particles hundreds of microns in diameter, as reported by Feely et al. [1990]. It is, of course, possible that such particles were present but too rare to be observed in our 140 mL samples and with our instrument sensitivity. Regardless, Feely et al. [1990] reported only the observed size *range* of plume particles, while it is the size *distribution* that is more important if we want to predict plume particle fate in a mass balance sense.

Extrapolation of the derived power-law size distribution to large particle diameters suggests that even if present, particles hundreds of microns in diameter would not have contributed a significant fraction of the total particulate mass at Beebe Vent. The contrast with the results of Feely et al. [1990] at Axial Seamount could be due to site-specific differences – for instance, the very high temperature reaction zone at the Piccard hydrothermal field [McDermott 2015]; the larger plume rise height, which could extend the vertical scale over which precipitation occurs; or different background-water entrainment ratios at the two sites due to different exit velocities and chimney heights [Jiang and Breier, 2014]. Our observations at Piccard caution against the

assumption of rapid deposition of hydrothermal, particulate metal fluxes, and illustrate the need for more particle size and composition measurements across a broader range of sites, globally.

5.4 Future applications of optical proxies in hydrothermal plume environments

The biogeochemical cycles active in buoyant hydrothermal plumes make compelling observational targets because of their potential basin-wide impacts [Breier et al., 2012; German and Seyfried, 2014]. A complete understanding of these cycles remains elusive due to the turbulence and spatiotemporal complexity of hydrothermal systems. We have demonstrated the previously untapped, but potentially valuable role, of optical sensing in these systems. Next steps in this field of research should include 1) closely correlated, discrete sampling programs to directly validate *in situ* optical proxies against established physical and biogeochemical methods; and 2) cross-validation of co-deployed sensors with variable spectral and scattering-angle sensitivities. This could optimally be achieved by interfacing *in situ* sensors with dedicated deep submergence vehicles, with attention paid to sampling geometries and ancillary measurements (e.g., temperature). Existing datasets including both side-scattering and beam attenuation may allow retroactive derivation of the $LSS:c_p(650)$ ratio described here. Well-validated use of the tools introduced here will allow the *in situ* characterization of particulate fluxes in hydrothermal plumes, at the spatiotemporal scales of biogeochemically important transformations.

6. Conclusion

In our field study at the Piccard Hydrothermal Field, Mid Cayman Rise, we have observed beam attenuation values at the Beebe Vents mound and in the overlying buoyant hydrothermal plume that exceed nearly all previously reported, calibrated measurements from throughout the world's

oceans. This includes prior studies associated with other high-temperature submarine vent systems. The magnitude of the optical scattering and attenuation coefficients suggest that, with proper validation, it should be more straightforward to extract information about particle size and composition at undersampled hydrothermal vents than in many well-studied, but low signal-to-noise, surface ocean environments. Particle size distributions immediately above the vent orifice exhibit among the steepest slopes ever observed, consistent with very small particle sizes freshly precipitating from actively rising and turbulently mixing vent fluids. This suggests that most particles pass through the initial precipitation zone in the buoyant hydrothermal plume without attaining settleable size. Our observations at Piccard caution against the general assumption of rapid deposition of hydrothermal, particulate metal fluxes. If gravitational settling is important for removal of material from plumes, then there must be subsequent aggregation into larger clusters which may act as a mechanism controlling the settling of material. We did not observe any evidence for large, solid, 100 μm particles as reported previously from other high-temperature vent systems [Feely et al. 1990]. Strong variability in the *in situ* ratio of optical sidescattering to beam attenuation over short vertical distances in the first 200 m of the rising plume, and intermittent departures from an otherwise strong relationship between total iron and beam attenuation, are consistent with the complex physical and chemical controls on particle size distributions and refractive index in young hydrothermal plumes.

Acknowledgements: Data presented in this publication are freely available upon request. This work was funded by the National Science Foundation (OCE-1029223; OCE-1061863), NASA (NNX09AB75G) and Woods Hole Oceanographic Institution's Deep Ocean Exploration Institute

and Ocean Ridge Initiative. Ship time (R/V *Falkor* cruise FK008) was funded by the Schmidt Ocean Institute and M.L.E. was supported by a WHOI Postdoctoral Scholar fellowship. The authors would like to thank the HROV *Nereus* technical team and the captain and crew of the R/V *Falkor* for shipboard support, and Emmanuel Boss (University of Maine) and Peter Traykovski (Woods Hole Oceanographic Institution) for the use of their optical sensors. C.R.G. also acknowledges the support of a Humboldt Research Award from the Alexander von Humboldt Foundation during the completion of this paper.

Accepted Article

References

- Agrawal, Y. C., and H. C. Pottsmith (2000), Instruments for particle size and settling velocity observations in sediment transport, *Marine Geology*, 168, 89–114.
- Agrawal, Y. C., A. Whitmire, O. A. Mikkelsen, and H. C. Pottsmith (2008), Light scattering by random shaped particles and consequences on measuring suspended sediments by laser diffraction, *Journal of Geophysical Research*, 113, doi:10.1029/2007JC004403.
- Baker, E. T., J. W. Lavelle, and G. J. Massoth (1985), Hydrothermal particle plumes over the southern Juan de Fuca Ridge, *Nature*, 316(6026), 342–344, doi:10.1038/316342a0.
- Baker, E. T., D. A. Tennant, R. A. Feely, G. T. Lebon, and S. L. Walker (2001), Field and laboratory studies on the effect of particle size and composition on optical backscattering measurements in hydrothermal plumes, *Deep Sea Research Part I: Oceanographic Research Papers*, 48(2), 593–604, doi: 10.1016/S0967-0637(00)00011-X.
- Bennett, S. A., E. P. Achterberg, D. P. Connelly, P. J. Statham, G. R. Fones, and C. R. German (2008), The distribution and stabilisation of dissolved Fe in deep-sea hydrothermal plumes, *Earth and Planetary Science Letters*, 270(3), 157–167.
- Bennett, S. A., P. J. Statham, D. R. H. Green, N. Le Bris, J. M. McDermott, F. Prado, O. J. Rouxel, K. Von Damm, and C. R. German (2011), Dissolved and particulate organic carbon in hydrothermal plumes from the East Pacific Rise, 9°50'N, *Deep Sea Research Part I: Oceanographic Research Papers*, 58(9), 922–931, doi:10.1016/j.dsr.2011.06.010.
- Boss, E., L. Guidi, M. J. Richardson, L. Stemann, W. Gardner, J. K. B. Bishop, R. F. Anderson, and R. M. Sherrell (2015), Optical techniques for remote and in-situ characterization of

- particles pertinent to GEOTRACES, *Progress in Oceanography*, 133(0), 43–54, doi:10.1016/j.pocean.2014.09.007.
- Boss, E., M. S. Twardowski, and S. Herring (2001a), Shape of the particulate beam attenuation spectrum and its inversion to obtain the shape of the particulate size distribution, *Applied Optics*, 40(27), 4885.
- Boss, E., W. S. Pegau, W. D. Gardner, J. R. V. Zaneveld, A. H. Barnard, M. S. Twardowski, G. C. Chang, and T. D. Dickey (2001b), Spectral particulate attenuation and particle size distribution in the bottom boundary layer of a continental shelf, *Journal of Geophysical Research*, 106(C5), 9509 – 9516.
- Boss, E., W. H. Slade, M. Behrenfeld, and G. Dall’Olmo (2009), Acceptance angle effects on the beam attenuation in the ocean, *Opt. Express*, 17(3), 1535–1550.
- Bowen, A. D. et al. (2008), The Nereus hybrid underwater robotic vehicle for global ocean science operations to 11,000 m depth, In *Proceedings of IEEE/MTS Oceans 2008*, Quebec.
- Breier, J. A., C. G. Rauch, K. McCartney, B. M. Toner, S. C. Fakra, S. N. White, and C. R. German (2009), A suspended-particle rosette multi-sampler for discrete biogeochemical sampling in low-particle-density waters, *Deep Sea Research Part I: Oceanographic Research Papers*, 56(9), 1579–1589.
- Breier, J. A., B. M. Toner, S. C. Fakra, M. A. Marcus, S. N. White, A. M. Thurnherr, and C. R. German (2012), Sulfur, sulfides, oxides and organic matter aggregated in submarine hydrothermal plumes at 9°50’N East Pacific Rise, *Geochimica et Cosmochimica Acta*, 88, 216–236, doi:10.1016/j.gca.2012.04.003.

- Breier, J.A., Sheik, C.S., Gomez-Ibanez, D., Sayre-McCord, R.T., Sanger, C.R., Rauch, Coleman, C.M., Bennett, S.A., Cron, B.R., Li, M., German, C.R., Toner, B.M., Dick, G.J., (2014), A large volume particulate and water multi-sampler with in situ preservation for microbial and biogeochemical studies, *Deep Sea Research Part I: Oceanographic Research Papers*, 94, 195–206, doi:10.1016/j.dsr.2014.08.008.
- Briggs, N., M. J. Perry, I. Cetinic, C. Lee, E. D'Asaro, A. M. Gray, and E. Rehm (2011), High-resolution observations of aggregate flux during a sub-polar North Atlantic spring bloom, *Deep Sea Research Part I: Oceanographic Research Papers*, 58(10), 1031–1039, doi:10.1016/j.dsr.2011.07.007.
- Cetinić, I., M. J. Perry, N. T. Briggs, E. Kallin, E. A. D'Asaro, and C. M. Lee (2012), Particulate organic carbon and inherent optical properties during 2008 North Atlantic Bloom Experiment, *Journal of Geophysical Research*, 117(C6), doi:10.1029/2011JC007771.
- Conway, T. M., and S. G. John (2014), Quantification of dissolved iron sources to the North Atlantic Ocean, *Nature*, 511(7508), 212–215, doi:10.1038/nature13482.
- Dick, G. J., K. Anantharaman, B. J. Baker, M. Li, D. C. Reed, and C. S. Sheik (2013), The microbiology of deep-sea hydrothermal vent plumes: ecological and biogeographic linkages to seafloor and water column habitats, *Frontiers in Microbiology*, 4, doi:10.3389/fmicb.2013.00124.
- Elderfield, H., and A. Schultz (1996), Mid-ocean ridge hydrothermal fluxes and the chemical composition of the ocean, *Annual Review of Earth and Planetary Sciences*, 24, 191–224.
- Feely, R. A., M. Lewison, G. J. Massoth, G. Robert-Baldo, J. W. Lavelle, R. H. Byrne, K. L. Von Damm, and H. C. Curl (1987), Composition and dissolution of black smoker particulates

- from active vents on the Juan de Fuca Ridge, *Journal of Geophysical Research: Solid Earth* (1978–2012), 92(B11), 11347–11363.
- Feely, R. A., T. L. Geiselman, E. T. Baker, G. J. Massoth, and S. R. Hammond (1990), Distribution and composition of hydrothermal plume particles from the ASHES Vent Field at Axial Volcano, Juan de Fuca Ridge, *Journal of Geophysical Research: Solid Earth*, 95(B8), 12855–12873, doi:10.1029/JB095iB08p12855.
- Fitzsimmons, J. N., E. A. Boyle, and W. J. Jenkins (2014), Distal transport of dissolved hydrothermal iron in the deep South Pacific Ocean, *Proceedings of the National Academy of Sciences*, 111(47), 16654–16661.
- Fitzsimmons, J. N., K. O. Forsch, R. M. Sherrell, and C. R. German (2014), A 4300 km-long particulate hydrothermal plume west of the southern East Pacific Rise: Particulate minor and trace elements from the US GEOTRACES Eastern Pacific Zonal Transect, *EOS Trans. AGU* Abst. OS23E-1277.
- Gartman, A., A. J. Findlay, and G. W. Luther (2014), Nanoparticulate pyrite and other nanoparticles are a widespread component of hydrothermal vent black smoker emissions, *Chemical Geology*, 366, 32–41, doi:10.1016/j.chemgeo.2013.12.013.
- Gartman, A., and G. W. Luther (2014), Oxidation of synthesized sub-micron pyrite (FeS₂) in seawater, *Geochimica et Cosmochimica Acta*, 144, 96–108, doi:10.1016/j.gca.2014.08.022.
- German, C. R., A. Bowen, M. L. Coleman, D. L. Honig, J. A. Huber, M. V. Jakuba, J. C. Kinsey, M. D. Kurz, S. Leroy, and J. M. McDermott (2010), Diverse styles of submarine venting on the ultraslow spreading Mid-Cayman Rise, *Proceedings of the National Academy of Sciences*, 107(32), 14020–14025.

- German, C. R., and R. S. J. Sparks (1993), Particle recycling in the TAG hydrothermal plume, *Earth and Planetary Science Letters*, 116(1–4), 129–134, doi:10.1016/0012-821X(93)90049-F.
- German, C. R. (ed.) (2014), *RV Falkor & ROV Nereus FK008 (Oases 2013) Cruise Report*, WHOI Internal Report.
- German, C. R., and W. E. Seyfried, Jr. (2014), Hydrothermal Processes, in *The Oceans and Marine Geochemistry*, vol. 6, pp. 191–233, Elsevier.
- Hatta, M., C. I. Measures, J. Wu, S. Roshan, J. N. Fitzsimmons, P. Sedwick, and P. Morton (2015), An overview of dissolved Fe and Mn distributions during the 2010–2011 U.S. GEOTRACES north Atlantic cruises: GEOTRACES GA03, *Deep Sea Research Part II: Topical Studies in Oceanography*, 116(0), 117–129, doi:10.1016/j.dsr2.2014.07.005.
- Hawkes, J. A., D. P. Connelly, M. Gledhill, and E. P. Achterberg (2013), The stabilisation and transportation of dissolved iron from high temperature hydrothermal vent systems, *Earth and Planetary Science Letters*, 375, 280–290, doi:10.1016/j.epsl.2013.05.047.
- Jackson, G. A., and A. B. Burd (1998), Aggregation in the Marine Environment, *Environ. Sci. Technol.*, 32(19), 2805–2814, doi:10.1021/es980251w.
- Jiang, H., and J. A. Breier (2014), Physical controls on mixing and transport within rising submarine hydrothermal plumes: A numerical simulation study, *Deep Sea Research Part I: Oceanographic Research Papers*, 92, 41–55, doi:10.1016/j.dsr.2014.06.006.
- Junge, C. E. (1969), Comments on “Concentration and Size Distribution Measurements of Atmospheric Aerosols and a Test of the Theory of Self-Preserving Size Distributions,” *J. Atmos. Sci.*, 26(3), 603–608, doi:10.1175/1520-0469(1969)026<0603:COASDM>2.0.CO;2.

- Kinsey, J. C., and C. R. German (2013), Sustained volcanically-hosted venting at ultraslow ridges: Piccard Hydrothermal Field, Mid-Cayman Rise, *Earth and Planetary Science Letters*, *380*, 162–168, doi:10.1016/j.epsl.2013.08.001.
- Kitchen, J. C., J. R. V. Zaneveld, and H. Pak (1982), Effect of particle size distribution and chlorophyll content on beam attenuation spectra, *Applied Optics*, *21*(21), 3913–3918.
- Klunder, M. B., P. Laan, R. Middag, H. J. W. De Baar, and J. C. van Ooijen (2011), Dissolved iron in the Southern Ocean (Atlantic sector), *Deep Sea Research Part II: Topical Studies in Oceanography*, *58*(25–26), 2678–2694, doi:10.1016/j.dsr2.2010.10.042.
- Klunder, M. B., P. Laan, R. Middag, H. J. W. de Baar, and K. Bakker (2012), Dissolved iron in the Arctic Ocean: Important role of hydrothermal sources, shelf input and scavenging removal, *Journal of Geophysical Research: Oceans*, *117*(C4), C04014, doi:10.1029/2011JC007135.
- Loisel, H., X. Meriaux, J.-F. Berthon, and A. Poteau (2007), Investigation of the optical backscattering to scattering ratio of marine particles in relation to their biogeochemical composition in the eastern English Channel and southern North Sea, *Limnol. Oceanogr.*, *52*(2), 739–752.
- McCave, I. N. (1984), Size spectra and aggregation of suspended particles in the deep ocean, *Deep Sea Research Part A. Oceanographic Research Papers*, *31*(4), 329–352, doi:10.1016/0198-0149(84)90088-8.
- McDermott, J. M. (2015), Geochemistry of deep-sea hydrothermal vent fluids from the Mid-Cayman Rise, Caribbean Sea, Ph.D. thesis, Massachusetts Institute of Technology/Woods Hole Oceanographic Institution, Woods Hole, MA.

- McNeil, G. T. (1977), Metrical Fundamentals of Underwater Lens System, *Optical Engineering*, 16(2), 128–162, doi:10.1117/12.7972089.
- Mikkelsen, O. A., T. G. Milligan, P. S. Hill, R. J. Chant, C. F. Jago, S. E. Jones, V. Krivtsov, and G. Mitchelson-Jacob (2008), The influence of schlieren on in situ optical measurements used for particle characterization, *Limnol. Oceanogr. Methods*, 6, 133–143.
- Neukermans, G., H. Loisel, X. Meriaux, R. Astoreca, and D. McKee (2012), In situ variability of mass-specific beam attenuation and backscattering of marine particles with respect to particle size, density, and composition, *Limnology and Oceanography*, 57(1), 124–144.
- Nishioka, J., H. Obata, and D. Tsumune (2013), Evidence of an extensive spread of hydrothermal dissolved iron in the Indian Ocean, *Earth and Planetary Science Letters*, 361(0), 26–33, doi:10.1016/j.epsl.2012.11.040.
- Ohnemus, D. C., and P. J. Lam (2015), Cycling of lithogenic marine particles in the US GEOTRACES North Atlantic transect, *Deep Sea Research Part II: Topical Studies in Oceanography*, 116(0), 283–302, doi:10.1016/j.dsr2.2014.11.019..
- Sander, S. G. and A. Koschinsky (2011), Metal flux from hydrothermal vents increased by organic complexation. *Nature Geosci.* 4, 145-150.
- Sands, C. M., D. P. Connelly, P. J. Statham, and C. R. German (2012), Size fractionation of trace metals in the Edmond hydrothermal plume, Central Indian Ocean, *Earth and Planetary Science Letters*, 319-320, 15–22, doi:10.1016/j.epsl.2011.12.031.
- Sedwick, P. N., J. A. Resing, B. M. Sohst, W. J. Jenkins, C. R. German, J. W. Moffett, A. Tagliabue (2014), Basic-scale transport of hydrothermal iron, manganese and aluminum across the eastern South Pacific. EOS Trans AGU abstr: OS22B-05.

Sheldon, R. W., A. Prakash, and W. H. Sutcliffe Jr (1972), The size distribution of particles in the ocean, *Limnology and Oceanography*, 327–340.

Stookey, L. L. (1970), Ferrozine-a new spectrophotometric reagent for iron, *Analytical Chemistry*, 42(7), 779–781.

Stramski, D., and D. A. Kiefer (1991), Light scattering by microorganisms in the open ocean, *Progress in Oceanography*, 28, 343–383.

Stramski, D., A. Bricaud, and A. Morel (2001), Modeling the inherent optical properties of the ocean based on the detailed composition of the planktonic community, *Applied Optics*, 40(18), 2929.

Sullivan, J. M., M. S. Twardowski, P. L. Donaghay, and S. A. Freeman (2005), Use of optical scattering to discriminate particle types in coastal waters, *Applied Optics*, 44(9), 1667.

Sullivan, J. M., M. S. Twardowski, J. R. V. Zaneveld, C. M. Moore, A. H. Barnard, P. L. Donaghay, and B. Rhoades (2006), Hyperspectral temperature and salt dependencies of absorption by water and heavy water in the 400-750 nm spectral range, *Appl. Opt.*, 45(21), 5294–5309.

Toner, B. M., S. C. Fakra, S. J. Manganini, C. M. Santelli, M. A. Marcus, J. W. Moffett, O. Rouxel, C. R. German, and K. J. Edwards (2009), Preservation of iron (II) by carbon-rich matrices in a hydrothermal plume, *Nature Geoscience*, 2(3), 197–201.

Twardowski, M. S., E. Boss, J. B. Macdonald, W. S. Pegau, A. H. Barnard, and J. R. V. Zaneveld (2001), A model for estimating bulk refractive index from the optical backscattering ratio and the implications for understanding particle composition in case I and case II waters, *Journal of Geophysical Research*, 106(C7), 14129 – 14142.

Voss, K. J. (1992), A spectral model of the beam attenuation coefficient in the ocean and coastal areas, *Limnol. Oceanogr*, 37(3), 501–509.

Walker, S. L., and E. T. Baker (1988), Particle-size distributions within hydrothermal plumes over the Juan de Fuca Ridge, *Marine Geology*, 78(3–4), 217–226, doi:10.1016/0025-3227(88)90110-7.

Wu, J., M. L. Wells, and R. Rember (2011), Dissolved iron anomaly in the deep tropical–subtropical Pacific: Evidence for long-range transport of hydrothermal iron, *Geochimica et Cosmochimica Acta*, 75(2), 460–468, doi:10.1016/j.gca.2010.10.024.

Yücel, M., A. Gartman, C. S. Chan, and G. W. Luther III (2011), Hydrothermal vents as a kinetically stable source of iron-sulphide-bearing nanoparticles to the ocean, *Nature Geoscience*, 4(6), 367–371.

Zaneveld, J. R. V., J. C. Kitchen, and C. M. Moore (1994), The scattering error correction of reflecting-tube absorption meters, in *Proceedings of SPIE*, vol. 2258, pp. 44–55.

Figure captions

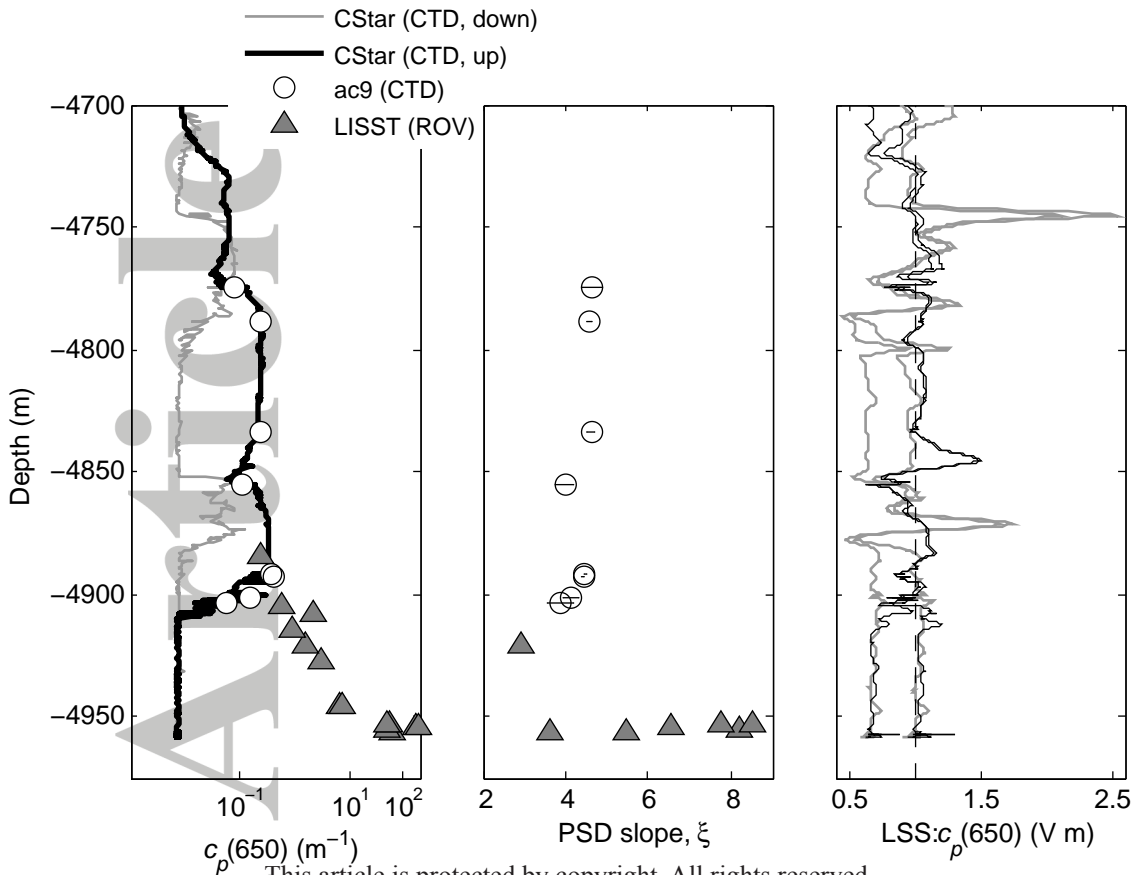
Figure 1. Profiles of optical proxies for concentration and size in the rising plume, measured in separate deployments from CTD and ROV platforms. *a)* *In situ* $c_p(650)$, a proxy for particle mass concentration, measured with the C-Star on the CTD during the upcast (black line) and downcast (gray line), $c_p(650)$ from CTD bottle samples measured on the ac9 (white circles), and $c_p(650)$ from SUPR-ROV bottle samples measured on the LISST (gray triangles). *b)* PSD slopes (ξ) of bottle samples (larger values correspond to smaller particles), inverted from γ measured using the ac9 on CTD bottle samples (white circles) and using the LISST on SUPR bottle samples (gray triangles). Low signal-to-noise in some LISST samples prevented estimation of ξ (see text). *c)* *In situ* ratio of scaled LSS to $c_p(650)$ on the upcast (black) and downcast (gray), computed from C-Star $c_p(650)$ and scaled side-scattering data as described in the text. Vertical dashed line marks a ratio of one. Paired black (upcast) and gray (downcast) lines show upper and lower uncertainty bounds propagated from sensor signal:noise. Where both lines fall to the left or right of the dashed line, the LSS: $c_p(650)$ ratio is significantly different than one. Ratios correspond to smaller particles and likely include some compositional effects (see text discussion).

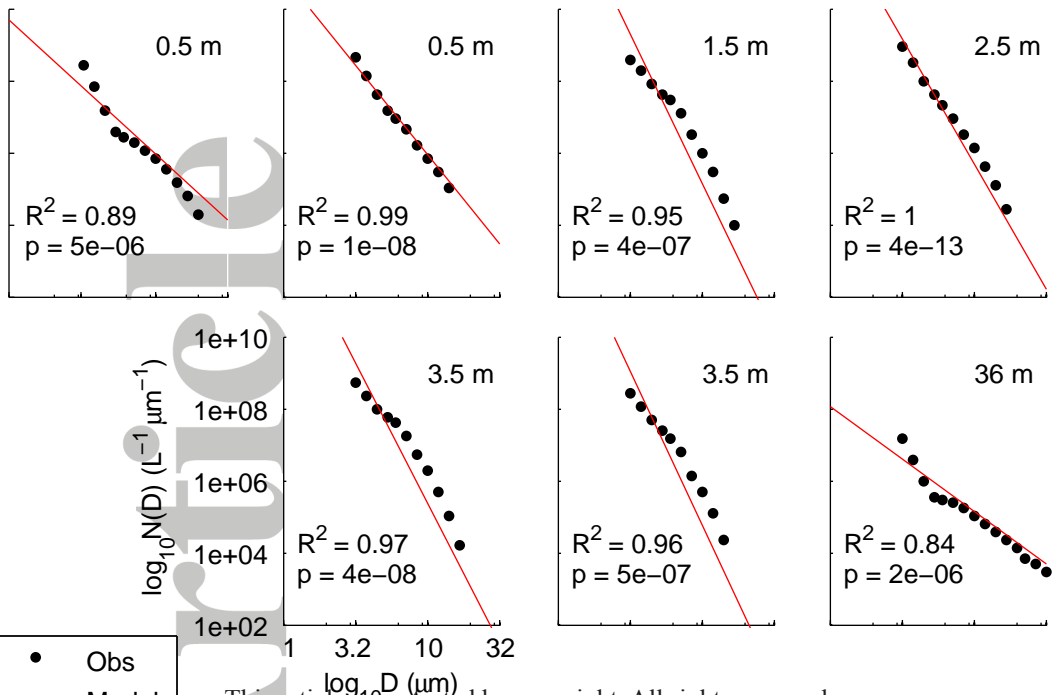
Figure 2. Number size distributions in ROV-SUPR bottle samples as measured with the LISST (black dots). Each panel shows one depth, as labeled. Also shown are the best-fit power-law models (fit only to data from size bins 5 μm and larger) and R^2 and p-values for the model vs. data. Departure from the power-law model is greatest in size bins less than approx. 5 μm .

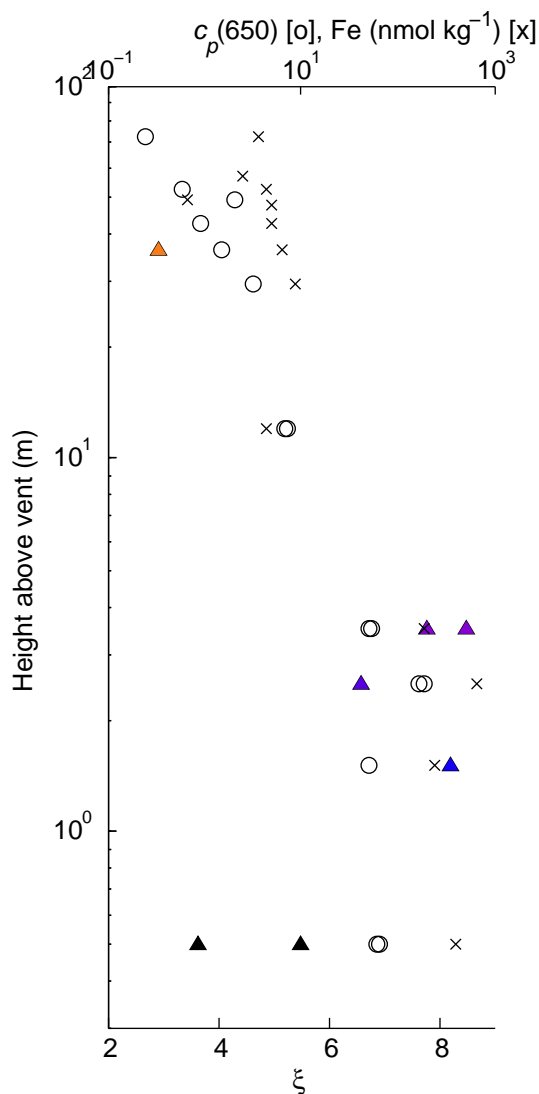
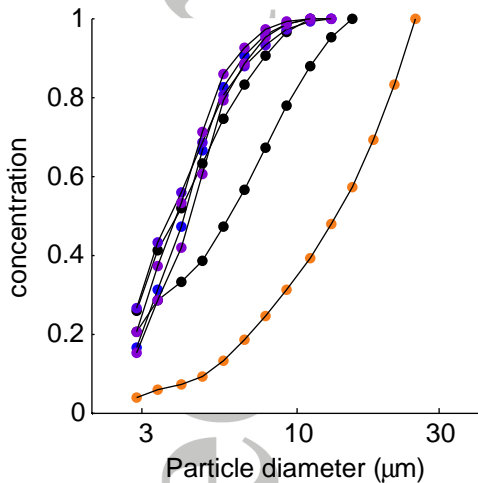
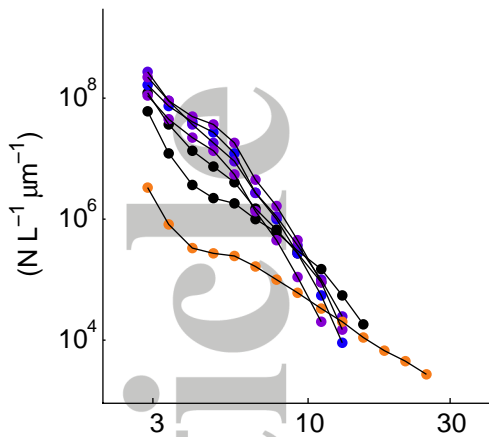
Figure 3. *a)* (top left) LISST number size distributions of particles in near-vent (0.5 – 37 m above the vent) SUPR-ROV bottle samples. *b)* (bottom left) As in panel a, but showing cumulative particle volume concentration, assuming solid, spherical particles. *c)* Profiles (vs. height above the vent) of best-fit values of ξ computed from LISST particle size spectra (colored triangles), $c_p(650)$ from the LISST (open circles), and whole-water iron concentration (crosses). Values of ξ are based on best fit to diameters above 5 μm . Logarithmic color scale applies to all panels and indicates height above the vent.

Figure 4. Scatter plots of $c_p(650)$ vs. whole-water iron concentrations measured in SUPR bottle samples in the rising plume above the Beebe Vents mound, Piccard Hydrothermal Field, Mid Cayman Rise. Colors on both panels reflect the height at which samples were taken above the vent-orifice. *a)* Left panel shows all data from 0.5 to 72.5 m, and Type II linear fit ($R^2 = 0.96$, $n = 14$). *b)* Right panel is zoomed in by a factor of 100 to show only the samples collected more than 25m off-bottom, together with the Type II linear fit to this restricted data set ($R^2 = 0.998$, $n = 6$). Samples shown with squares were not included in that linear fit.

Figure 5. Spectral albedo (the fraction of beam attenuation accounted for by scattering ($b(\lambda)$) rather than absorption) of suspended, powdered iron oxide and sulfide mineral standards in water. Absorption accounts for a greater fraction of beam attenuation by sulfide minerals, than it does for oxide minerals. Measurements were collected with an ac-9 in the laboratory, and data were processed and corrected similarly to field data described in the text. Particle maximum diameters are given in the legend.

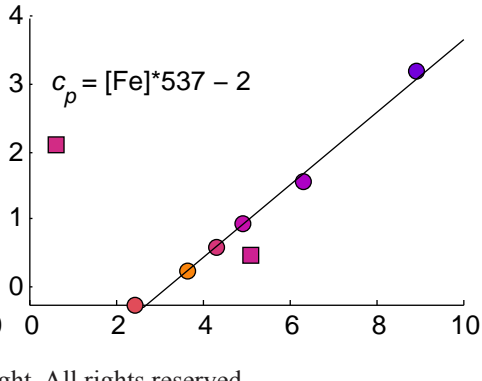
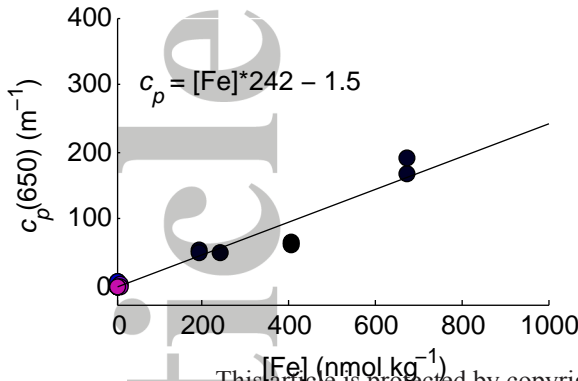






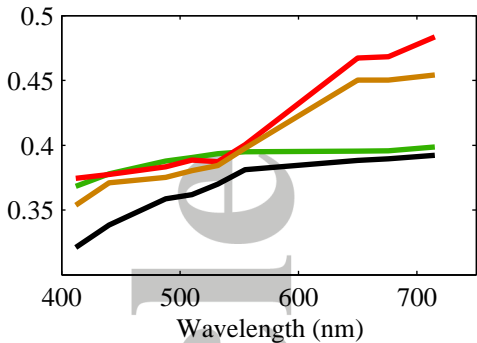
Height above vent (m)

0 20 40 60



[Fe] (nmol kg⁻¹)

This article is protected by copyright. All rights reserved.



Chalcopyrite < 90 μ m

Pyrrhotite < 90 μ m

Hematite < 90 μ m

Ferrihydrite < 12 μ m